Improved State Estimation in Distorted Magnetic Fields

Christian Brommer[1], Christoph Böhm[2], Jan Steinbrener[3], Roland Brockers[4] and Stephan Weiss[5]

***Abstract*—The magnetic field of the Earth – besides varying naturally – may be disturbed locally by the (man-made) environment. State estimation and corresponding navigation frameworks that use magnetometers on-board of mobile platforms suffer from severe performance loss or failure upon local magnetic distortions if these are not detected and mitigated adequately. Advanced estimators include the magnetic variation in the state vector. However, Cartesian coordinates, although widely used in the literature, suffer from observability issues when it comes to disturbance detection. This paper shows the importance of representing the magnetic variation in a spherical coordinate system and subsequent improvements with respect to the common representation in Cartesian coordinates. The spherical representation improves estimator consistency and allows for accurate and fast mitigation of magnetic disturbances through consistent statistical tests which leads to better system state estimates in magnetically distorted areas. The approach is validated by performing tests with simulated and real-world data on embedded hardware.**

I. Introduction

The magnetic field of the Earth exhibits local variations both in terms of direction and magnitude that occur either naturally or are induced by artificial structures and devices. These variations can lead to significant errors in state estimation for magnetometer based navigation frameworks if the effects are not taken into account. While magnetic variations that occur naturally can be approximated and hard-coded based on georeferenced look-up tables (such as provided by the International Geomagnetic Reference Field (IGRF)), variations due to man-made structures in the vicinity need to be assessed dynamically and online. This paper shows that dynamic and statistically correct assessment of the magnetic field improves both navigation/state estimation and outlier handling.

Current approaches that estimate the local magnetic field rely on Cartesian coordinates for the representation of the magnetic field. This work proposes an approach that estimates the local magnetic variation and detects disturbances in the magnetic field with a consistency improved estimation process based on spherical coordinates. The presented approach allows uninterrupted state estimation and adaptation to local magnetic disturbances, especially for platforms such as Unmanned Aerial Vehicles (UAV) that move over far distances, which causes significant changes in the magnetic field. This approach focuses on the improvement of the statistical signal properties and the observability of the magnetic field as well as extrinsic sensor calibration. The method utilizes a natural magnetometer data representation in spherical coordinates (in contrast to the widely used Cartesian definition), which allows the direct estimation and improved consistency of the observable components. Thus, the introduced method improves the overall accuracy of the state estimation process and allows for the correct detection of disturbances in the magnetic field. The consistency of the covariance estimation is further improved by adapting the sensor-model and moving non-linear transformations outside the estimation process. Reducing non-linear components of the sensor-model especially improves the performance of statistical tests, such as χ^2 for detecting signal disturbances. To support our findings and the approach, we compare different sensor update models with aspects on the statistical distribution of their input-data, their consistency, and the performance of applied outlier rejections both in simulation and with real-world data. The improved measurement update, disturbance detection, and adaptation to the disturbed environment were implemented in C++ by utilizing and extending the existing EKF based state estimation framework presented in [1]. In the final step, the implementation is also deployed on an Odroid XU4 ARM embedded platform.

Control of Networked Systems Group, Universität Klagenfurt.
[1]christian.brommer@ieee.org, [2]christoph.boehm@ieee.org,
[3]jan.steinbrener@aau.at,[5]stephan.weiss@ieee.org
Jet Propulsion Laboratory, California Institute of Technology.
[4]brockers@jpl.nasa.gov
The research leading to these results has received funding from the Austrian Ministry for Transport, Innovation and Technology (BMVIT) under grant agreement n. 855777 (MODULES) and from the ARL within the BAA W911NF-12-R-0011 under grant agreement W911NF-16-2-0112.
Post-print version, accepted April/2020, DOI follows ASAP ©IEEE.

II. Related Work

Using a magnetometer to improve the attitude estimation of an Extended-Kalman-Filter (EKF) is not new to the robotic community. This topic is addressed by various methods such as linear regression [2], vector alignment by using accelerometer data, and the horizontal component of the magnetic vector for a Gauss-Newton Quaternion approach [3], [4], [5]. Several approaches limit the information that is provided by the magnetic sensor to the horizontal plane and normalize the magnitude of the magnetic field [6]. Such methods reduce the sensitivity against magnetic disturbances but neglect the information of the third dimension and the magnetic field strength. The presented approach goes one step further by introducing a sensor model that uses all three dimensions of the sensor information, decomposed into two angles and the magnetic field strength. It improves the accuracy of the attitude estimation and rejection of outliers.

The above work does not detect magnetic anomalies or rejects such anomalies as outliers before the filter update step. Some methods use error margins on the update residual [7], or statistical tests [8] to reject measurements, but they do not adapt to areas with a disturbed magnetic field. The proposed

method extends the previous work with a novel approach that includes the magnitude of the magnetic field, which is used to detect environmental disturbances and to modify states for the extrinsic magnetometer calibration to adapt to the current magnetic environment.

Advanced approaches such as presented by [2] and [9] use a high number of magnetic sensors that are placed in strategic locations to detect and compensate magnetic disturbances. An approach presented by [10] uses machine learning to determine the expected distortion of the local magnetic field for a moving robot. These approaches require significant computational power, and additional space for the increased sensor setup, which is not suitable for miniaturized vehicles such as UAV's and can not mitigate long-term field disturbances. The presented method uses a single magnetometer and a computationally efficient EKF to process magnetic information in an accurate and consistent way as well as in real-time on a resource-constrained platform. In this work, we are investigating the benefits of a more natural representation of the magnetic field information. While the majority of the existing approaches interpret the magnetic information as a 3D vector in Cartesian space, the work of [11], [12], and the approach presented in this paper use a spherical representation of the magnetic information. While the work of [11] and [12] only uses spherical coordinates to represent the magnetic field, we make full use of the representation in our filter framework and show that the presented method successfully mitigate disturbances and improve state estimation, both in simulation and real-world experiments.

III. Magnetometer State Estimation

A. Probability Distribution

This section presents the differences of the magnetic state definition ${}_w\mathbf{m}$ in Cartesian coordinates ${}_w\mathbf{m}_{cart} = [x, y, z]^\mathsf{T}$ and spherical coordinates ${}_w\mathbf{m}_{spher} = [r, \theta, \varphi]^\mathsf{T}$. We use the notation C2S$(\cdot)$ and S2C$(\cdot)$ respectively to transform between the Cartesian and spherical space (see Figure 1). In both representations, the magnetic field vector is represented in the GPS global reference frame (thus, the y- and θ-elements will be non-zero because of the magnetic declination with respect to the GPS frame). A goodness of fit test was performed on real-world data for the spherical and Cartesian representation in order to determine if the spherical representation is beneficial in view of a Gaussian distribution. A 3-Axis digital HMC5843 magneto-resistive sensor was used to record real-world data. The raw measurement of the sensor is provided in the Cartesian form with unit [Counts], which is directly proportional to the magnetic field strength [Tesla]. Thus, the conversion of the measurement to Tesla does not have a benefit over using the raw sensor information. The dataset for this test scenario was recorded in a stationary setup over a period of 2.2 hours with a measurement rate of 60 Hz.

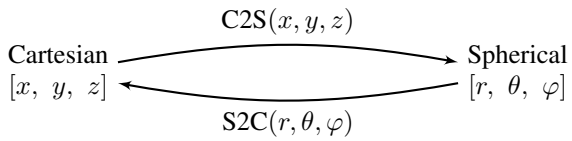

Fig. 1. Conversion naming between Cartesian to spherical representation.

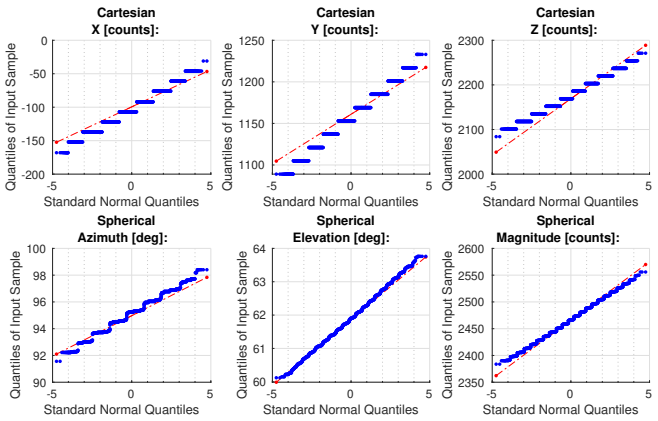

Fig. 2. Evaluation of the measurement sample distribution (blue data points) in spherical and Cartesian form. QQ-Plots are used to compare the Cartesian measurement samples x, y and z in the top three plots and spherical measurement samples for azimuth, elevation, and magnitude in the bottom three plots. The closer the measurement samples are to the red reference line, the closer is the signal to the normal distribution hypothesis. The direct comparison confirms that the spherical form of the same dataset is more Gaussian distributed than the Cartesian data.

The standard deviation and mean are shown in Table I. A Quantil-Quantil-Plot (QQ-Plot) as shown in Figure 2 was used to determine which representation is closer to a Gauss distributed hypothesis. QQ-Plots are evaluated visually and are more robust against numerical issues such as quantization or measurement discretization in comparison to a χ^2 test.

Figure 2 shows the QQ-Plot of real-world magnetometer data and visualizes both, quantization, and measurement discretization effects. The plots provide a reference line that represents the relationship of sample quantiles and the expected theoretical quantiles for a normal distribution. The Gaussianity is evaluated based on how linear the measurement samples are, and how close the measurement samples are to the reference line of the hypothesis. The closer these measurement samples are to this line, the closer is the sample distribution to normality. The raw Cartesian measurement samples are shown in the upper plots of Figure 2. The clustering of the data points arise due to discretization caused by the Analog-Digital-Converter (ADC) of the sensor. The same raw Cartesian measurement samples are used to calculate spherical measurements. The results for the spherical measurement samples are presented at the bottom of Figure 2 and show less discretization due to this transformation. A comparison of the plots for the Cartesian and spherical measurement representation confirms that the raw measurements of the magnetometer match a normally distributed hypothesis closer in the case of the spherical representation. For this reason, the spherical representation does generally benefit

TABLE I
Standard deviation and mean of the real-world dataset.

	Mean	STD
Spherical		
Azimuth [deg]	95.116	0.725
Elevation [deg]	61.885	0.415
Magnitude [Counts ($\propto$ Tesla)]	2466.039	19.823
Cartesian [Counts ($\propto$ Tesla)]		
x	-103.622	14.668
y	1157.296	16.293
z	2175.026	21.162

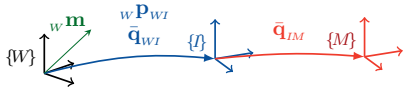

Fig. 3. Setup of the frames and transformations of the system. W represents the World frame, I the IMU/body frame and M the magnetometer frame on-board the mobile platform. The magnetic vector ${}_{W}\mathbf{m}$ is expressed in the ENU world frame.

statistical filtering processes that rely on the assumption of normally distributed signals. In the following sections, we implemented this approach based on a readily available EKF[1] framework [1] to confirm the benefits of the spherical state representation over the widely used Cartesian form.

B. EKF State and Update

We use the following notation: the translation ${}_{A}\mathbf{p}_{BC}$ defines frame C with respect to frame B expressed in frame A. The translation is expressed in frame B if the subscript A is not defined. The quaternion $\bar{\mathbf{q}}_{AB}$ describes the rotation of frame B with respect to frame A. $\mathbf{C}(\bar{\mathbf{q}}_{AB}) \equiv \mathbf{C}_{AB}$ denotes the conversion of quaternion $\bar{\mathbf{q}}_{AB}$ to its corresponding direction cosine matrix. Please note that this work uses the Hamilton notation for the Quaternion representation [13]. The individual frames of the system are defined in Figure 3.

The EKF framework uses an Inertial-Measurement-Unit (IMU) for the propagation of the state formulation defined by Eq. (1). The essential core states are the position of the IMU/body frame $\mathbf{p}_{WI}$ expressed w.r.t the world frame, velocity $\mathbf{v}_{WI}$, the orientation of the IMU in the world frame $\bar{\mathbf{q}}_{WI}$, gyroscopic bias $\mathbf{b}_\omega$ and accelerometer bias $\mathbf{b}_a$. ${}_{W}\mathbf{m}$ represents the magnetic field in the East-North-Up (ENU) world frame, the extrinsic magnetometer calibration $\bar{\mathbf{q}}_{IM}$ is expressed w.r.t. the IMU frame and magnetic measurements are expressed in the magnetometer frame M. The y-axis of the world frame is oriented towards the geographic north (ENU) as GPS systems generally use it. The full state vector $\mathbf{X}$ is defined as follows:

$$\mathbf{X} = \left[\mathbf{p}_{WI}^\mathsf{T}, \mathbf{v}_{WI}^\mathsf{T}, \bar{\mathbf{q}}_{WI}^\mathsf{T}, \mathbf{b}_\omega^\mathsf{T}, \mathbf{b}_a^\mathsf{T}, \bar{\mathbf{q}}_{IM}^\mathsf{T}, {}_{W}\mathbf{m}^\mathsf{T}\right]^\mathsf{T} \tag{1}$$

The magnetic world frame M is not aligned with the ENU world frame W due to the magnetic declination. Magnetic declination is the angle between the magnetic north and the true north which varies depending on the location thus introducing a misalignment. The filter estimates the local magnetic declination because ${}_{W}\mathbf{m}$ is defined as a measurement of the magnetic field with respect to the ENU world frame W. The system dynamics of the core states are defined according to [1]. The dynamics and process noise of the additional magnetometer state ${}_{W}\mathbf{m}$ and extrinsic $\bar{\mathbf{q}}_{IM}$ are assumed as zero because the declination of the local magnetic field is expected to be short term constant between two propagation steps (i.e. IMU reading). The EKF framework uses an error state definition with $\delta\boldsymbol{\theta}_{AB}$ describing a small angle error rotation of B w.r.t frame A and the skew-symmetric matrix of a vector $\mathbf{A}$ is defined as $[\mathbf{A}]_\times$. ${}_{W}\boldsymbol{\Delta}\mathbf{m}$ describes the error of the magnetic state w.r.t. the world frame and $\widetilde{\mathbf{z}}$ is the residual for the error state.

[1]A UKF implementation may be less sensitive (not immune) to non-Gaussian distributed signals but has other application-dependent drawbacks.

$$\hat{\mathbf{z}} = \hat{\mathbf{C}}_{IM}^\mathsf{T}\hat{\mathbf{C}}_{WI}^\mathsf{T}\,{}_{W}\hat{\mathbf{m}}_{cart} \tag{2}$$

$$\mathbf{z} = (\hat{\mathbf{C}}_{IM}(\mathbf{I} + [\delta\boldsymbol{\theta}_{IM}]_\times))^\mathsf{T}\,(\hat{\mathbf{C}}_{WI}(\mathbf{I} + [\delta\boldsymbol{\theta}_{WI}]_\times))^\mathsf{T} \quad (\,{}_{W}\boldsymbol{\Delta}\mathbf{m}_{cart} + {}_{W}\hat{\mathbf{m}}_{cart}) \tag{3}$$

$$\widetilde{\mathbf{z}}_{cart} = \mathbf{z} - \hat{\mathbf{z}} \tag{4}$$

The Cartesian state update formulation is shown in Equations (2), (3) and (4). It can be seen that the magnetic state information is directly rotated into the magnetometer frame resulting in non-linear transformations for each component.

The raw magnetometer measurements that are utilized for the Cartesian and spherical state definitions are expressed in the Cartesian form. The raw measurement needs to be converted to spherical coordinates prior to the update of the spherical state representation. The residual is then calculated in spherical space Eq. (7). The update formulation for the spherical case is shown by Equations (5), (6) and (7). The spherical residual in Eq. (7) contains less non-linear transformations and supports the findings of Section III-A. In particular, the spherical representation allows a direct estimation of the magnitude of the magnetic field, and the update is thus linear. Therefore, the spherical representation has less non-linear parameters. The two non-linear components $h_1(\mathbf{X}), h_2(\mathbf{X})$ contain state variables as a combination of rotations and skew-symmetric matrices. While the resulting expression is too long to be presented in its individual components, $h_1(\mathbf{X}), h_2(\mathbf{X})$ essentially rotate a unit vector.

$$\hat{\mathbf{z}} = \text{C2S}(\hat{\mathbf{C}}_{IM}^\mathsf{T}\hat{\mathbf{C}}_{WI}^\mathsf{T}\,\text{S2C}({}_{W}\hat{\mathbf{m}}_{spher})) \tag{5}$$

$$\mathbf{z} = \text{C2S}((\hat{\mathbf{C}}_{IM}(\mathbf{I} + [\delta\boldsymbol{\theta}_{IM}]_\times))^\mathsf{T}\,(\hat{\mathbf{C}}_{WI}(\mathbf{I} + [\delta\boldsymbol{\theta}_{WI}]_\times))^\mathsf{T} \quad \text{S2C}({}_{W}\boldsymbol{\Delta}\mathbf{m}_{spher} + {}_{W}\hat{\mathbf{m}}_{spher})) \tag{6}$$

$$\widetilde{\mathbf{z}}_{spher} = \mathbf{z} - \hat{\mathbf{z}} = \left[\;\Delta r, h_1(\mathbf{X}), h_2(\mathbf{X})\;\right]^\mathsf{T} \tag{7}$$

Because of angular definitions, the azimuth and elevation updates needs to be within limits of the spherical definition $(0 \leqslant \theta \leqslant \pi,\ 0 \leqslant \varphi < 2\pi,\ 0 \leqslant r)$ to prevent singularities.

C. Observability

An observability analysis, according to [14] was performed for the full state as defined by Eq. (1) and its dynamics as described by [1]. The analysis of the described system showed that magnetometer and inertial readings alone do not render the orientation of a mobile system fully observable; position $\mathbf{p}_{WI}$, velocity $\mathbf{v}_{WI}$ and accelerometer bias $\mathbf{b}_a$ are also unobservable. This is expected since no position, or velocity update information is provided. According to our analysis, gyroscopic bias $\mathbf{b}_\omega$ and the extrinsic calibration of the magnetometer $\bar{\mathbf{q}}_{IM}$ are fully observable, and the magnetometer states $\bar{\mathbf{q}}_{WI}$ and ${}_{W}\mathbf{m}$ are jointly observable (following the definition of joint observability in [15], [16])[2]. The system can

[2]Example of joint observability: If two states span a 2D space with only one observable dimension, this dimension is a linear combination of the two states and the unobservable dimension is perpendicular to it [15], [14]. If information, which is orthogonal to the observable dimension, is added (e.g. knowing a state of the two), both states become observable as the information spans now the full 2D state space. As such, joint observability *imposes a defined constraint on the joint behavior* of the involved states.

TABLE II
NULLSPACE OF THE OBSERVABILITY ANALYSIS - **CARTESIAN STATE** (SEE EQUATION (2)).

$q_{w,wi}$	$q_{x,wi}$	$q_{y,wi}$	$q_{z,wi}$	m_x	m_y	m_z
J1	J1	J1	0	J1	J1	0
J2	J2	J2	0	J2	0	J2

TABLE III
NULLSPACE OF THE OBSERVABILITY ANALYSIS - **SPHERICAL STATE**. (SEE EQUATION (5)).

$q_{w,wi}$	$q_{x,wi}$	$q_{y,wi}$	$q_{z,wi}$	m_{az}	m_{el}	m_r
J1	J1	J1	J1	J1	J1	0
J2	J2	J2	J2	J2	J2	0

be extended by a position sensor that contributes the so-called pseudo attitude [17] and renders the orientation observable. This is not within the scope of the presented method, and no position information was introduced for the presented work.

The magnetic field vector states span a space of three dimensions with two unobservable dimensions and one observable dimension (of course, this is independent of the state representation as a state transformation does not change input or output of the system). The Cartesian state formulation in Table II shows the individual results for the states (columns) and unobservable dimensions (rows). The blue elements (J1/J2) represent two unobservable dimensions, which renders rotation quaternion states and magnetic field vector states jointly observable states. It is not apparent which state is observable for the Cartesian case (see Tab. II) whereas the results for the spherical formulation in Table III shows that the magnitude of the spherical vector ${}_W\mathbf{m}_{spher}$ (green column) is the fully observable dimension in the magnetic field vector sub-state-space. The table further shows that the azimuth and elevation of the magnetic field vector remain only jointly observable with the rotation of the IMU $\bar{\mathbf{q}}_{WI}$, these states form two unobservable dimensions in the state space.

Naturally, the observability information *per se* does not change with the state or measurement *representation* but the spherical form allows a clear interpretation of the physical relations. It further provides the magnitude as a directly measured/observable state which improves the convergence of the mean, covariance and consistency of the filter. Figure 4 shows the magnetic state error for the Cartesian x, y and z states which do not converge and take fixed arbitrary values with high covariances (> 100). In contrast, the covariance of their norm converges correctly, which shows the defined behavior according to their joint observability. Equations (8), (9) and (10) are used to transform the covariance of the Cartesian state components to the covariance for their norm (P_n). Please note that the scales of the y-axis for the two graphs are different.

$$f_n(x, y, z) = \sqrt{x^2 + y^2 + z^2} \tag{8}$$

$$F_n = \frac{\delta f(x, y, z)}{\delta [x, y, z]^\mathsf{T}} \tag{9}$$

$$P_n = F_n P_c F_n^\mathsf{T} \tag{10}$$

D. Setup for the Simulated Dataset

A 10 minute simulated dataset with the same signal characteristics as the real magnetic sensor, mentioned in Section III-A, was generated for the test of covariance validation and disturbance detection. The signal characteristics include the frequency of the measurement (50 Hz magnetometer and 200 Hz IMU), the sample noise of the magnetic sensor and magnetic variation of the environment. The noise of the simulated magnetometer measurement is additive, normally distributed, zero mean sample noise with the same standard deviation (STD) as the real measurement (see Table I). This noise is added to the ground truth data in the Cartesian form such that the noise for the Cartesian case is normally distributed and not distorted. This is done to prevent disadvantages for the Cartesian filter scenario. Given the noise perturbed data, and a setting that rejects outliers outside of the 3σ bounds, we expect, that a fully consistent estimator detects 0.27% of the samples as outliers.

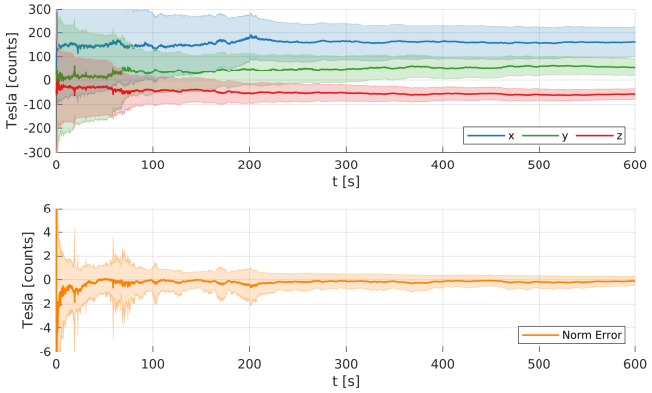

Fig. 4. Comparison of the individual Cartesian components and their estimation error (solid lines) with respect to the post-calculated norm and corresponding 3σ bounds (transparent bands) of the transformed covariance. The individual components (x, y, z) take arbitrary values and do not converge as they have a high covariance while the norm converges to a narrow covariance bound (note the different scales of the y-axis). The (x, y, z) components are jointly observable: they span a three dimensional space with only one observable dimension (their norm).

We apply this value in the following for the comparison of the experimental results. We are using a simulated dataset without measurement disturbances and a second dataset with an introduced measurement disturbance in the form of a step function. The disturbance is added in Cartesian space $(x + 100,\ y + 10$ and $z + 10)$ which corresponds to an equivalent disturbance in spherical space $(\theta + 0.1°,\ \varphi + 0.1°$ and $r + 101)$ at $t = 300\,\text{s}$.

E. Disturbance Detection and Covariance Validation

The correct estimation of the state covariance is important for reliable outlier detection. Outliers can be caused by single measurement errors or disturbances in the magnetic field, which affects the measurement over a longer period of time. The disturbance detection utilizes a χ^2 test based on the residual y and its covariance S during the EKF update Eq. (11). For comparison, the disturbance detection is performed for three scenarios:

- Directly on the Cartesian state components (x, y, z),
- the covariance of the norm for the Cartesian state by using the error propagation law Eq. (10), and
- the magnitude of the spherical state representation.

TABLE IV
OUTLIER DETECTION RESULTS FOR THE SIMULATED DATASETS

Test case	Detections vs. Measurements [%]
3 Sigma	$1 - 99.73\% = 0.27\%$
Cartesian Norm	1.14%
Spherical Magnitude	0.21%
Cartesian XYZ	0.14%

$$S = HPH^{\mathsf{T}} + R \tag{11}$$

$$S_n = F_n \left(HPH^{\mathsf{T}}\right) F_n^{\mathsf{T}} + F_n R F_n^{\mathsf{T}} \tag{12}$$

$$= F_n \left(HPH^{\mathsf{T}} + R\right) F_n^{\mathsf{T}} \tag{13}$$

$$= F_n S F_n^{\mathsf{T}} \tag{14}$$

The χ^2 value (Eq. 16) is compared to the "upper critical value" (ucv) to define outlier ($\chi^2 >$ ucv). The probability value (p-value) for the ucv is set to $1 - 3\sigma = 0.27\%$. The ucv depends on the p-value and degrees of freedom. The Cartesian norm has three degrees of freedom (x, y, z), while the spherical formulation has one degree of freedom in the form of the magnitude r. The ratio of χ^2 detections with respect to the number of measurements is a measure for the confidence of the filtering process. The evaluation for the three filter scenarios is shown in Table IV. The conducted tests used the same simulated dataset and the individual filter did not perform outlier *rejections* only *detection*. The results of the Cartesian states (x, y and z) show under-confident behavior based on the number of detections far below the expected 3σ bound. This is due to inconsistencies and high covariance estimates because the state is not directly observable. Results on the Cartesian norm, on the other hand, show a high number of detections exceeding the expected value. This over-confidence is caused by non-linear transformations during the calculation of the residual and its covariance, which leads to numerous false positives. The number of outliers for the spherical state is slightly below 3σ but clearly the closest to the expected value. The noise of the dataset is added in Cartesian space and subsequently transformed into the spherical space, which causes a distorted and not normal distributed noise. This presents a disadvantage (by design) for the spherical formulation, which still outperforms the Cartesian scenario.

F. State Covariance Adjustment

A disturbance is defined by a sequence of more than 10 consecutive outlier detections equal to a timespan of 200 ms at 50 Hz. Active adjustments of the covariance are performed if a disturbance is detected. The corrections of the covariance are designed to enclose the current measurement, which was declared as a disturbance due to the affected local magnetic field, by a 1σ bound. This allows the correct convergence of the filter and adaptation to the new magnetic field at the current location. Due to this adjustment, the correct estimation can be maintained despite the magnetic distortion and without decreasing the overall estimation performance. The update of the spherical magnitude is a linear and direct update defined by $H_{spher(1,1)} = 1$ of the 3x3 Jacobian (Eq. (15)).

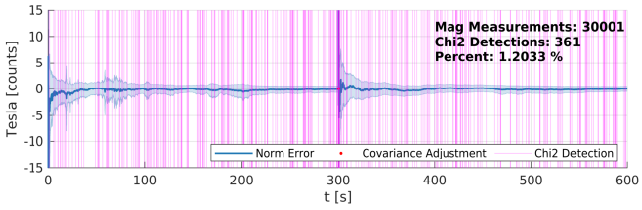

Fig. 5. The norm (solid blue line) of the *Cartesian state* with 3σ bounds of the corresponding covariance (transparent blue bands). Magenta vertical lines show the χ^2 detections based on the *norm of the Cartesian* $x, y,$ and z states. The 361 detections (1.2%) are above the expected detection rate (0.27%) due to the over-confidence of the filter in this setup. The over-confidence causes a high number of false positives.

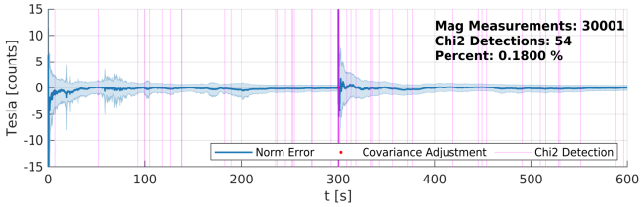

Fig. 6. The norm (solid blue line) of the *Cartesian state* with 3σ bounds of the corresponding covariance (transparent blue bands). Magenta vertical lines show the χ^2 detections based on the $x, y,$ and z states. The 54 detections (0.18%) are below the expected detection rate (0.27%) due to the under-confidence of the filter in this setup.

$$H_{spher} = \begin{bmatrix} 1 & 0 & 0 \\ 0 & H_{spher(2,2)} & H_{spher(2,3)} \\ 0 & H_{spher(3,2)} & H_{spher(3,3)} \end{bmatrix} \tag{15}$$

Equation (18) is used to calculate the covariance adaptation based on the current residual y, measurement noise R, and χ^2 value. The new χ^2 value to enclose the disturbance is calculated using a quantile function to determine the upper critical value for 1σ. This method is only applicable to the magnitude of the spherical formulation because of the scalar entry in the Jacobian $H_{spher(1,1)}$. Further simplification because of the linear transformation leads to Equation (18) which is derived from Equations (16) and (11). The dynamic adjustment for the Cartesian definition requires the calculation of the 3x3 covariance matrix based on the scalar χ^2 value, which represents a "one-to-many" problem. The covariance for the Cartesian case is therefore set to $\sigma = 200$ (the same value used for initialization of the state covariance matrix) to allow for viable fast convergence.

$$\chi^2 = \frac{y^2}{\sigma^2} \tag{16}$$

$$P = H^{\dagger}\left(\sigma^2 - R\right)\left(H^{\mathsf{T}}\right)^{\dagger} = H^{\dagger}\left(\frac{y^2}{\chi^2} - R\right)\left(H^{\mathsf{T}}\right)^{\dagger} \tag{17}$$

$$\Rightarrow P = \frac{y^2}{\chi^2} - R, \text{ with: } H = 1,\ H^{\dagger}\text{: Pseudoinverse} \tag{18}$$

The three tests on the covariance are performed with simulated data and an introduced interference at $t = 300$ s as described in Section III-D. The covariance is adapted after 10 consecutive outliers while no outlier rejection is performed. The χ^2 test for Cartesian components (Fig. 5) detected 1.2% of the measurements as outliers which is five times higher than the expected 3σ bound (0.27%). False positives can lead to wrong disturbance detections in real-world applications,

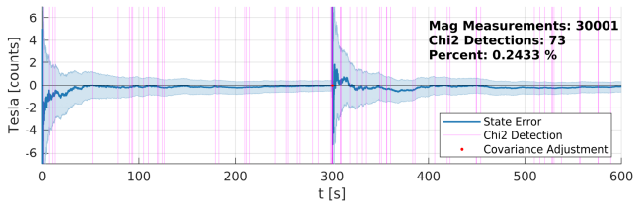

Fig. 7. Magnitude (solid blue line) of the *spherical state* with 3σ bounds of the corresponding covariance (transparent blue bands). Magenta vertical lines show the χ^2 detections based on the *magnitude* of the magnetic field. The 73 detections (0.24%) are close to the expected detection rate (0.27%).

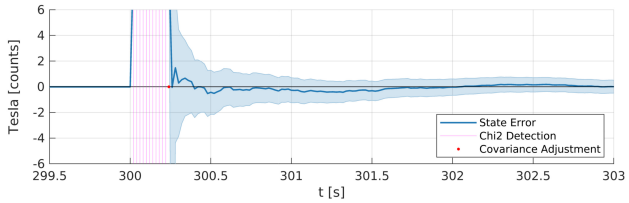

Fig. 8. This plot shows the magnitude (solid blue line) of the spherical state and its covariance (transparent blue bands). The covariance is adjusted based on the χ^2 test that detected the disturbance at $t = 300\,\mathrm{s}$. The state converges to the new value after 1.5 seconds and the error decreases rapidly.

as presented in Section IV. The post processed covariance of the Cartesian norm, based on Eq. (8) is shown by (Fig. 6) and detects only 0.18% as outliers. Figure 7 illustrates the same experiment for the spherical state representation. The number of outliers is 0.24%, which is close to the expected value of 0.27%. The filter correctly converges to the disturbed state 1.5 seconds after the adjustment. Figure 8 shows a zoom of the region with the covariance adjustment. The three scenarios detect the disturbance correctly, which is expected for the high magnitude that was applied for the interference.

IV. Experimental Results

The real-world dataset was recorded with the vehicle (AscTec Hummingbird) that was used for the noise analysis in Table I. The magnetometer was calibrated to compensate for hard iron effects [18] using a correction based on an ellipsoid fit. The device was carried arbitrarily over a parking lot with randomly introduced orientations and no intentional magnetic disturbances. The recorded data provides 100 Hz IMU, 60 Hz magnetometer readings and 20 Hz RTK GPS position provided by a Trimble BD930-UHF. The position measurement is used to associate interferences with their geographical location (see Figure 9). The filter was setup with the same noise and state covariance initialization as for the simulated data. The attitude states are initialized based on the gravity and the magnetic field vector using [19] to ensure a fair comparison of the Cartesian and spherical state representation. The filter did reject measurements based on the χ^2 test to reflect the correct application in a real-world scenario. The evaluation of the real-world data was performed on the Cartesian state definition with outlier detection on the norm and for the spherical state definition, which performs the outlier detection on the magnitude. An evaluation based on the individual Cartesian states x, y, z was not pursued since these states are not directly observable. Just as in simulation, the results of the Cartesian filter formulation (Fig. 10) shows incorrect χ^2 detections due to the over-confidence of the filter resulting in incorrect covariance adjustments. The

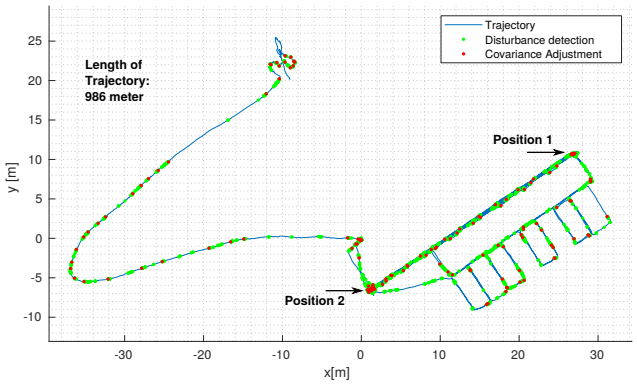

Fig. 9. 2D position plot of the real-world dataset illustrating the 986 meter trajectory that was used for the final results. The χ^2 detections and covariance adaptations are determined by using the filter with the spherical state representation.

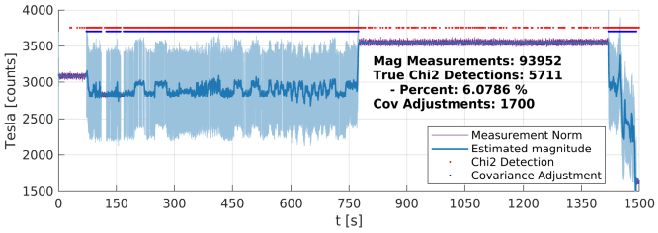

Fig. 10. This plot shows the results of the real-world data evaluation using the Cartesian state definition (5711 detections (6.07%)). The χ^2 test uses the norm of the states for the outlier detection and rejection. It can be seen that the outlier rejections for the over-confident filter causes numerous false positives for the adjustment of the covariance.

proposed spherical representation shown in Figure 11 detects magnetic disturbances correctly and adapts rapidly to the disturbed field. This corroborates the results obtained with the simulated data described in Section III-F. Figures 12 and 13 show a zoomed segment between seconds 150 and 300 of Figures 10 and 11. The magnified segments show a distinct and repeated change of the magnetic field, which correlates to a geographical interpretation between the labeled positions one and two in Figure 9. The path between these positions is the exact trajectory that was followed four times during this period. As a result, we can verify that the disturbance in these two locations is persistent, and the presented method detects the change of the magnetic field in this area reliably. The presented method can be verified because the disturbance detection is reproducible with real-world data.

Besides performing the tests on a workstation, the same data was also successfully processed in real-time with the C++ framework on an Odroid XU4 embedded platform. The processing time of the update with spherical representation is

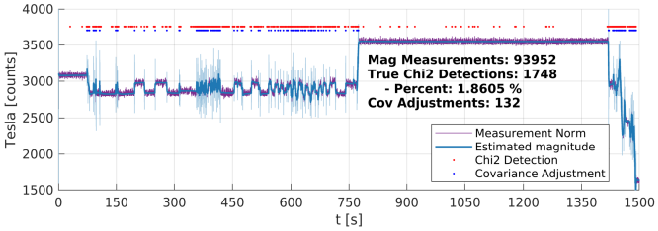

Fig. 11. This plot shows the results of the real-world data evaluation using the spherical state definition (1748 detections (1.86%)). It can be seen that the correct outlier detection and rejection for the magnitude of the magnetic field leads to an improved state estimation.

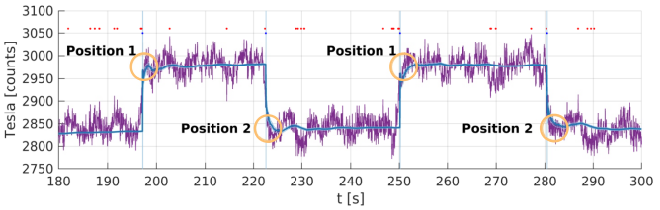

Fig. 12. Segment of the processed real-world dataset which used the spherical state representation for filtering and the magnitude state for χ^2 detections. The plot (legend as in Fig.11) shows four detections that match with two distinct positions in the geographical plot shown in Figure 9.

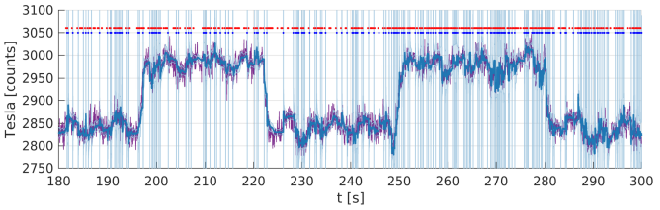

Fig. 13. Segment of the real-world dataset which used the Cartesian state formulation and the norm of the Cartesian states for the χ^2 detection. The plot (legend as in Fig.11) shows numerous false positives for the disturbance detection. This filter formulation is over-confident as shown in Section III-E. The over-confidence causes numerous false positives of the χ^2 detections and subsequent covariance adjustments. These adjustments cause the filter to follow even the noise in the measurement. Conversely, not acting on the detections would cause the filter to ignore the long-term disturbances and, thus, also lead to poor state estimation performance.

3.71 ms on the embedded platform and 0.4 ms on a workstation allowing a possible magnetometer update rate of 2500 Hz on the workstation and 270 Hz on the embedded platform.

V. Conclusions

Using a spherical state formulation over a Cartesian representation reveals the full information contained in the jointly observable states of the system. The raw measurement shows a more Gaussian distributed noise if expressed in spherical coordinates. The spherical state formulation renders the magnitude of the magnetic field directly observable in comparison to the jointly observable states of the Cartesian state definition. This formulation improves the covariance estimation thus improves the outlier detection based on a χ^2 test that relies on a Gaussian assumption. The accurate outlier detection further allows the active covariance adjustment in order to accustom to the magnetically disturbed environment. The results confirm that the presented method, which uses a spherical state formulation, is more accurate in estimating the state covariance in comparison to the Cartesian representation that is widely used in the robotics community. The EKF that was used for the experiments did benefit from the reduced non-linearity and better Gaussian distribution of the spherical measurement representation. Robotic-platforms that travel far distances such as UAVs commonly have limited computational power, and EKFs are regularly used because of their increased performance compared to other methods. The method was successfully tested on the described embedded hardware with real-world data. A reliable attitude estimation can be achieved if the presented method is combined with a position sensor. This combination renders the orientation of the mobile system observable and allows the estimation of the magnetic variation. The proposed approach proved the correct adaptation to local magnetic disturbances throughout the conducted evaluations and improved the reliability of the state estimation.

Acknowledgment

A portion of the research was carried out at the Jet Propulsion Laboratory, California Institute of Technology, under a contract with the National Aeronautics and Space Administration (80NM0018D0004).

References

[1] S. Weiss, M. W. Achtelik, M. Chli, and R. Siegwart, "Versatile distributed pose estimation and sensor self-calibration for an autonomous mav," in *2012 IEEE International Conference on Robotics and Automation*, May 2012, pp. 31–38.

[2] L. Christensen, C. Gaudig, and F. Kirchner, "Distortion-robust distributed magnetometer for underwater pose estimation in confined uuvs," in *OCEANS 2015 - MTS/IEEE Washington*, Oct. 2015, pp. 1–8.

[3] J. L. Marins, , E. R. Bachmann, R. B. McGhee, and M. J. Zyda, "An extended kalman filter for quaternion-based orientation estimation using marg sensors," in *Proceedings 2001 IEEE/RSJ International Conference on Intelligent Robots and Systems*, vol. 4, Oct. 2001, pp. 2003–2011.

[4] A. Chan, S. Tan, and C. Kwek, "Sensor data fusion for attitude stabilization in a low cost quadrotor system," in *2011 IEEE 15th International Symposium on Consumer Electronics (ISCE)*, Jun. 2011, pp. 34–39.

[5] R. Munguia and A. Grau, "Attitude and heading system based on ekf total state configuration," in *2011 IEEE International Symposium on Industrial Electronics*, Jun. 2011, pp. 2147–2152.

[6] S. Sabatelli, M. Galgani, L. Fanucci, and A. Rocchi, "A double-stage kalman filter for orientation tracking with an integrated processor in 9-d imu," *IEEE Transactions on Instrumentation and Measurement*, vol. 62, no. 3, pp. 590–598, Mar. 2013.

[7] H. G. de Marina, F. J. Pereda, J. M. Giron-Sierra, and F. Espinosa, "Uav attitude estimation using unscented kalman filter and triad," *IEEE Transactions on Industrial Electronics*, vol. 59, no. 11, pp. 4465–4474, Nov. 2012.

[8] P. A. Miller, J. A. Farrell, Y. Zhao, and V. Djapic, "Autonomous underwater vehicle navigation," *IEEE Journal of Oceanic Engineering*, vol. 35, no. 3, pp. 663–678, Jul. 2010.

[9] V. Renaudin, M. H. Afzal, and G. Lachapelle, "New method for magnetometers based orientation estimation," in *IEEE/ION Position, Location and Navigation Symposium*, May 2010, pp. 348–356.

[10] L. Christensen, M. Krell, and F. Kirchner, "Learning magnetic field distortion compensation for robotic systems," in *2017 IEEE/RSJ International Conference on Intelligent Robots and Systems (IROS)*, vol. 2017-Septe, Sep. 2017, pp. 3516–3521.

[11] M. Abdelrahman and S. Y. Park, "Simultaneous spacecraft attitude and orbit estimation using magnetic field vector measurements," *Aerospace Science and Technology*, vol. 15, no. 8, pp. 653–669, 2011.

[12] J. K. Deutschmann and I. Y. Bar-Itzhack, "Evaluation of Attitude and Orbit Estimation Using Actual Earth Magnetic Field Data," *Journal of Guidance, Control, and Dynamics*, vol. 24, no. 3, pp. 616–623, 2001.

[13] H. Sommer, I. Gilitschenski, M. Bloesch, S. Weiss, R. Siegwart, and J. Nieto, "Why and how to avoid the flipped quaternion multiplication," *Aerospace*, vol. 5, no. 3, p. 72, Jul. 2018.

[14] R. Hermann and A. Krener, "Nonlinear controllability and observability," *IEEE Transactions on Automatic Control*, vol. 22, no. 5, pp. 728–740, Oct. 1977.

[15] A. Martinelli, "Continuous Symmetries and Observability Properties in Autonomous Navigation," INRIA, Research Report RR-7049, 2010.

[16] S. M. Weiss, "Vision based navigation for micro helicopters," Ph.D. dissertation, ETH Zurich, 2012. [Online]. Available: http://hdl.handle.net/20.500.11850/52698

[17] R. P. Kornfeld, R. J. Hansman, and J. J. Deyst, "Single-Antenna GPS-Based Aircraft Attitude Determination," *Navigation*, vol. 45, no. 1, pp. 51–60, Mar. 1998.

[18] C. Konvalin, "Compensating for tilt, hard-iron, and soft-iron effects," *Sens. Mag*, vol. 26, pp. 1–11, 12 2009.

[19] R. Valenti, I. Dryanovski, and J. Xiao, "Keeping a good attitude: A quaternion-based orientation filter for IMUs and MARGs," *Sensors*, vol. 15, no. 8, pp. 19 302–19 330, Aug. 2015.